Sādhanā Vol. 42, No. 4, April 2017, pp. 467–477
DOI 10.1007/s12046-017-0622-z

Numerical simulation of breakup and detachment of an axially stretching Newtonian liquid bridge with a moving contact line phase field method

KISHORE SINGH PATEL and RATNESH K SHUKLA*

Department of Mechanical Engineering, Indian Institute of Science, Bangalore 560012, India
e-mail: ratnesh@mecheng.iisc.ernet.in

MS received 19 May 2016; revised 8 October 2016; accepted 20 October 2016

Abstract. The extensional, breakup and detachment dynamics of an axially stretching Newtonian liquid bridge are investigated numerically with a dynamic domain multiphase incompressible flow solver. The multiphase flow solver employs a Cahn–Hilliard phase field model to describe the evolution of the diffuse interface separating the liquid bridge fluid from the surrounding medium. The governing axisymmetric Navier–Stokes and Cahn–Hilliard phase field equations are discretized on a continuously expanding domain, the boundaries of which coincide with the planar solid surfaces containing the liquid bridge. The entire formulation, including the fast pressure correction for high density ratios and the semi-implicit discretization that overcomes the numerical stiffness of the fourth-order spatial operators, is performed on a fixed simplified computational domain using time-dependent transformation. Simulations reveal that the dynamic domain interface capturing technique effectively captures the deformation dynamics of the stretching liquid bridge, including the capillary wave formation, necking and interface evolution post breakup and detachment. It is found that the liquid bridge detachment is strongly influenced by the contact angle prescribed at the stationary and moving solid surfaces. At relatively small pulling speeds, the entire liquid is found to preferentially adhere to the less hydrophobic surface. When the prescribed contact angles are equal, however, the liquid bridge undergoes complete detachment so that no liquid resides either on the stationary or on the moving solid surface.

Keywords. Liquid bridge; multiphase incompressible flows; contact line; phase field method.

1. Introduction

Liquid bridges that are invariably formed during breakup and coalescence of droplets are frequently observed in a variety of engineering and day-to- day life process such as printing and lubrication for industrial application, colouring of fibres, wall coating for domestic applications, etc. [1]. Depending on the relative importance of the viscous, inertial and surface tension forces, the deformation and thinning dynamics of continuously stretched liquid bridges can generally be classified into inertial thinning, viscocapillary and viscocapillary–inertial regimes. Due to the fundamental importance of liquid bridge dynamics in several physical and technological processes, these three regimes, including a fluctuation-dominated regime for nanoscale liquid threads, have been the subject of numerous theoretical, experimental and computational investigations.

While the early focus of theoretical investigations was on prediction of equilibrium profiles and quantification of the forces exerted by the liquid bridge on the confining solid boundaries [2, 3], more recent works have analysed the continuum singularity close to necking and eventual pinch-off through one-dimensional models. These continuum models that are derived from asymptotic approximations for long slender threads [4, 5] assume radial variations to be negligibly small and employ empirical relationships for the moving contact line to account for the variations in the axial velocity and bridge radius in time.

The extensional dynamics of stretched liquid bridges have also been extensively investigated through numerical simulations (see Kumar [1] for a review). The moving solid boundary and the shear-free liquid–air interface are most naturally handled in an arbitrary Lagrangian–Eulerian (ALE) framework that allows for continuous deformation of the computational domain, the boundaries of which coincide with the moving surface and shear-free surface, in time. It is therefore no surprise that a vast majority of simulation-based investigations of liquid bridge dynamics utilize the ALE [6, 7] method with the finite-element grid adaptation [8, 9]. ALE methods rely on the smoothness of boundary to achieve superior accuracy and in principle can be utilized only before singular merger or breakup events.

*For correspondence

Beyond these events, application of robust remeshing and surgical tools that remove the mesh irregularity artificially becomes inevitable. Moreover, the unstructured grid that is used for discretization in ALE must also be remeshed with each step of time advancement to account for the motion of the solid boundary containing the liquid bridge. The necessity of frequent remeshing increases the computational expense of ALE methods substantially and can also result in a degradation in accuracy owing to the errors associated with interpolation between original and remeshed grids.

In the Cartesian grid framework, the immersed boundary and immersed interface methods offer an alternative way of accounting for the motion of the solid boundary containing the liquid bridge on a fixed structured Cartesian mesh (e.g., Marella *et al* [10]). Typically, these methods rely on interface capturing techniques (level set method for instance) that robustly handle large topological variations in the multifluid interface. Note, however, that to account for the continuous motion of the solid boundaries, these methods still require frequent interpolation between the mesh points over successive time instants. Such interpolation adversely impacts the overall solution accuracy [11, 12].

For relatively straightforward boundary motion, such as those encountered in the case of liquid bridges confined between planar solid boundaries, a rather simplified approach of employing time-dependent transformations that map the deforming domain on to a fixed Cartesian domain seems possible. Such a cost-effective approach would alleviate problems associated with frequent remeshing and interpolation, which are necessary in the case of ALE or immersed boundary methods. Moreover, it is desirable to have a simulation methodology that allows for investigation of liquid bridge dynamics in more general settings that could involve background shear and more than two components [1]. In this work we pursue such an approach of utilizing time-dependent transformations that account for the physical motion of the boundary that coincides with the moving solid surface and thus perform interface capturing multiphase flow simulations on a fixed computational domain discretized using simple Cartesian mesh. Furthermore, since our simulation method employs field functions to distinguish between various fluid components, it can be easily extended to configurations that involve three or more phases. The fact that the flow field is solved for in both the liquid bridge interior and the surrounding medium implies that our method is applicable to configurations that involve time-dependent background flow.

Our interface capturing approach is based on the Cahn–Hilliard phase field method and employs a diffuse mesh-resolved interface function (phase field) the width of which is comparable to the mesh spacing. In the past, similar interface capturing methodologies that rely on field equations for the scalar interface function have been shown to accurately describe interfacial dynamics in both compressible and incompressible multicomponent flows [13–17]. The fact that this interface capturing method remains robust, even when large topological changes across material interfaces involving high density ratios (as in the case of water liquid bridge in air medium for instance) are encountered, makes it especially well suited for investigating extensional and detachment dynamics of axially stretched liquid bridges. Furthermore, the Cahn–Hilliard phase field method also allows for a simplified treatment of the moving contact line. Note that accounting for the contact line motion in a sharp interface framework is significantly more challenging, owing to the stress singularity that results from the incompatibility between the no-slip boundary condition and the motion of the sharp contact line. A majority of the investigations assume that the contact lines are pinned and not permitted to move across the solid–liquid boundary [18, 19]. Typically, to overcome the stress singularity, the no-slip boundary condition must be relaxed in the vicinity of the wetting line through prescription of Navier slip boundary condition with a length parameter that determines the length scale of the region beyond which the no-slip boundary condition is recovered [9, 20, 21]. In contrast, the presence of diffusive transport across the fluid–fluid interface in our present Cahn–Hilliard phase-field-model-based diffuse interface framework enables effective elimination of the unphysical stress singularity, and leads to finite viscous dissipation at the moving contact line [22, 23].

The organization of this paper is as follows. The flow configuration of an axially stretching liquid bridge confined between a stationary lower and moving upper plate is described in section 2 along with the governing equations for the evolution of flow field and the fluid–fluid interface. The discretization methodology and the interface capturing technique are described in section 3. Results from the simulations on liquid bridge stretched axially between two hydrophobic surfaces that are continuously pulled apart are presented in section 4 before the conclusions.

2. Problem specification and governing equations

Figure 1 depicts a schematic of the set-up under consideration. A liquid bridge is located initially between two planar hydrophobic surfaces. The contact angle at the bottom stationary plate is given by θ_{bottom} with θ_{top} as the one prescribed at the top moving plate. The top plate is pulled upwards along the axial direction at a constant speed of V_c. The resulting deformation, detachment and breakup of the liquid bridge are assumed to be axisymmetric with z denoting the axis of symmetry in the cylindrical coordinate system (r, z).

The flow and the interface motion resulting from the pulling action of the upper plate are governed by the

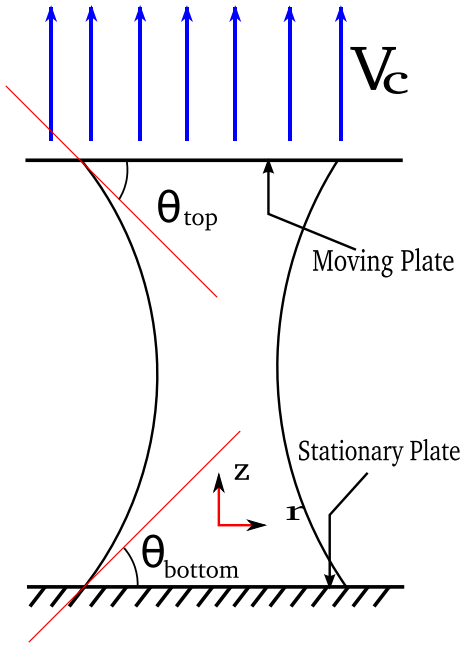

Figure 1. Schematic depicting the liquid bridge formed between two planner surfaces where θ_{top} and θ_{bottom} represent the contact angles for the *moving top* and *stationary bottom plates*, respectively, while V_c denotes the pulling velocity of the top plate.

following incompressible Navier–Stokes Cahn–Hilliard equations:

$$\nabla \cdot \mathbf{u} = 0, \tag{1a}$$

$$\rho \frac{\partial \mathbf{u}}{\partial t} + (\rho \mathbf{u} \cdot \nabla)\mathbf{u} = -\nabla p + \nabla \cdot [\mu(\nabla \mathbf{u} + \nabla \mathbf{u}^T)] + G\nabla\phi, \tag{1b}$$

$$\frac{\partial \phi}{\partial t} + \nabla \cdot (\phi u) = M\nabla^2 G. \tag{2}$$

Equation (2) represents the dimensional form of the Cahn–Hilliard phase field model for the phase field ϕ that assumes asymptotic values of -1 and 1 in the interior of the liquid bridge and the surrounding medium, respectively. The sharp interface that separates the two phases is given by the zero isocontour of ϕ. In Eq. (2), M represents the mobility parameter while G denotes the chemical potential. Moreover, G can be expressed as a variational derivative of the total free energy F as [13]

$$G = \frac{\delta F}{\delta \phi} s = \frac{3\sigma}{2\sqrt{2}\epsilon}(\phi^3 - \phi - \epsilon^2 \nabla^2 \phi), \tag{3}$$

where σ denotes the surface tension coefficient and the parameter ϵ is directly proportional to the interface width. Furthermore, the Cahn number $Cn = \epsilon/L$ with L as the characteristic length scale. The phase field function ϕ assumes the a hyperbolic tangent functional form and thus decays exponentially to its asymptotic limits of ± 1 away from the sharp fluid–fluid interface given by $\phi = 0$. The fluid density and viscosity are given by

$$\rho(\phi) = \frac{(1+\phi)}{2}\rho_a + \frac{(1-\phi)}{2}\rho_l, \tag{4a}$$

$$\mu(\phi) = \frac{(1+\phi)}{2}\mu_a + \frac{(1-\phi)}{2}\mu_l, \tag{4b}$$

where ρ_a and ρ_l, and, μ_a and μ_l represent the densities and viscosities of the pure fluid components, respectively, with subscripts l and a denoting liquid bridge fluid and air, respectively.

The computational domain is fixed such that its lower and upper boundaries coincide with the bottom stationary and the top moving plates, respectively. To account for the motion of the upper boundary, we adopt a generalized coordinate transformation approach [24], wherein the continuously expanding physical domain (r, z) is mapped onto a time-invariant computational domain (ζ, η).

Here, since only the upper boundary of the physical domain undergoes prescribed time-dependent motion, the following coordinate relationship can be established between the physical and the computational domains:

$$r = \zeta, \tag{5a}$$

$$z = \eta\left(1 + \frac{g(t)}{L_0}\right), \tag{5b}$$

$$t = \tau, \tag{5c}$$

where $g(t)$ determines the movement of the top domain boundary with L_0 as the initial domain length (or equivalently initial liquid bridge length) along the axial z direction. The set of governing equations [Eqs. (1) and (2)] are transformed onto the computational domain using transformation metrics. In general, the transformation metrics themselves must satisfy the discrete geometrical conservation laws [25], which preserve freestream uniform flow conditions exactly. In the present case, the spatially uniform Jacobian of the transformation (J) is given by

$$J = r_\zeta z_\eta - r_\eta z_\zeta = 1 + \frac{g(t)}{L_0}. \tag{6}$$

The transformed governing equations in the computational domain are given by

$$\nabla \cdot \mathbf{u} = 0, \tag{7a}$$

$$\rho\left[\frac{\partial(J\mathbf{u})}{\partial t} + \nabla \cdot (J\mathbf{u}\mathbf{u}) - \frac{\partial(\eta g'(t)\mathbf{u}/L_0)}{\partial \eta}\right] = -J\nabla p + \nabla \cdot [J\mu(\nabla \mathbf{u} + \nabla \mathbf{u}^T)] + J(RHS), \tag{7b}$$

$$\frac{\partial(J\phi)}{\partial t} + \nabla\cdot(J\mathbf{u}\phi) - \frac{\partial(\eta g'(t)\phi/L_0)}{\partial\eta} = \frac{M}{Cn}J\nabla^2(\phi^3 - \phi - Cn^2\nabla^2\phi), \tag{7c}$$

where the $J(RHS)$ term that accounts for the surface tension force and body forces is given by

$$J(RHS) = JG\nabla\phi + J\rho(\phi)\mathbf{g}, \tag{8}$$

with $\mathbf{g}$ as the acceleration due to gravity. The gradient, divergence and Laplacian operators in the transformed coordinate system are given by

$$\nabla = \hat{\zeta}\frac{\partial}{\partial\zeta} + \hat{\eta}\frac{1}{J}\frac{\partial}{\partial\eta}, \tag{9a}$$

$$\nabla^2 = \frac{\partial^2}{\partial\zeta^2} + \frac{1}{\zeta}\frac{\partial}{\partial\zeta} + \frac{1}{J}\frac{\partial}{\partial\eta}\left(\frac{1}{J}\frac{\partial}{\partial\eta}\right). \tag{9b}$$

The overall dynamics of the liquid bridge and its eventual breakup and detachment depend strongly on the prescribed contact angle and pinning and depinning of the contact line [26]. To account for the contact line motion we prescribe the following boundary conditions on the upper and lower boundaries:

$$\mathbf{u} = \mathbf{u}_s, \tag{10a}$$

$$\mathbf{n}\cdot\nabla G = 0, \tag{10b}$$

$$\frac{1}{J}\frac{\partial\phi}{\partial\eta} = \frac{\cos\theta_s(1-\phi^2)}{Cn\sqrt{2}}, \tag{10c}$$

where $\mathbf{u}_s$ and θ_s denote the prescribed velocity and contact angle, respectively. The subscript s denotes the appropriate solid surface corresponding to the lower or upper boundaries (e.g., $\theta_s = \theta_{top}$ on the upper boundary). Note that our prescription of a fixed contact angle corresponds to an ideal surface that is free of surface heterogeneities, which typically cause the advancing and receding contact angles to deviate from the static contact angle. Moreover, as evidenced from the results presented in section 4, the apparent contact angle is found to vary significantly with the contact line motion even though the contact angle at the solid surface is kept fixed at its prescribed value. At the lateral boundaries of the computational domain, outflow boundary conditions are prescribed by forcing the normal velocity gradients to vanish identically.

3. Simulation methodology

We perform a conservative finite-volume discretization of the transformed governing equations on a fully staggered grid arrangement. The scalar quantities, namely the phase field function ϕ, pressure, viscosity and density are defined at cell centres while the velocities are located at intercell boundaries. For spatial approximation, we employ standard second-order accurate central differencing for the diffusion terms with a Minmod-reconstruction-based upwind approximation for the convective terms.

The incompressible Navier–Stokes equations are solved using a second-order accurate projection method [27–29]. To overcome the numerical stiffness of the linear viscous terms, momentum equations are discretized semi-implicitly through a combination of Adams–Bashforth and Crank–Nicolson integrators as follows:

$$\frac{(J\mathbf{u})^* - (J\mathbf{u})^n}{\Delta t} = \frac{1}{\rho^{n+1}}\left\{\left[\frac{3}{2}\mathbf{N}^n - \frac{1}{2}\mathbf{N}^{n-1}\right] + \frac{1}{2\rho^{n+1}}\left[\mathbf{L}(\mu^{n+1},\mathbf{u}^*,J^{n+1}) + \mathbf{L}(\mu^n,\mathbf{u}^n,J^n)\right]\right\} \tag{11}$$

$$\frac{(J\mathbf{u})^{n+1} - (J\mathbf{u})^*}{\Delta t} = -\frac{1}{\rho^{n+1}}\nabla(Jp)^{n+1}. \tag{12}$$

In these expressions, $\mathbf{L}$ represents the linear diffusion operators with $\mathbf{N}$ as the nonlinear operator that includes both the convection as well as surface tension terms.

Equation (12) yields a variable-coefficient Poisson-like equation for the pressure field, which must be solved at each step of the flow evolution. Presence of variable density terms in the elliptic equation (12) for the pressure results in an ill-conditioned linear system. To alleviate numerical instability resulting from this ill-conditioning at high density contrasts, we split the variable-coefficient elliptic operator into a constant coefficient type following prior work of Dodd and Ferrante [30] as follows:

$$\frac{1}{\rho^{n+1}}\nabla(Jp)^{n+1} \longrightarrow \frac{1}{\rho_c}\nabla(Jp)^{n+1} + \left(\frac{1}{\rho^{n+1}} - \frac{1}{\rho_c}\right)\nabla(J^{n+1}\tilde{p}), \tag{13}$$

where $\tilde{p} = 2p^n - p^{n-1}$ and $\rho_c = \min(\rho_1, \rho_2)$ is a constant. This splitting simplifies computations significantly as the variable-coefficient linear equation for the pressure field is converted into a constant-coefficient Poisson equation given below:

$$\frac{1}{\rho_c}\nabla^2(Jp)^{n+1} = \nabla\cdot\left[\left(\frac{1}{\rho^{n+1}} - \frac{1}{\rho_c}\right)\nabla(J^{n+1}\tilde{p})\right] + \frac{\nabla\cdot(J^{n+1}\mathbf{u})^*}{\Delta t}. \tag{14}$$

Equation (14) can be easily solved with standard efficient direct solvers such as the one based on matrix diagonalization method [29].

An additional difficulty arises from the fact that the Cahn–Hilliard phase field equation for ϕ involves fourth-order spatial operators so that stringent restrictions on the maximum allowable time step size (from the CFL criterion) are encountered for explicit temporal integrators. To overcome the numerical stiffness arising from the presence of

fourth-order spatial operators in Eq. (7c) and thus maintain numerical stability for reasonably large time steps, we devise splitting techniques similar to the ones suggested in prior works (e.g., Badalassi *et al* [31]). Since we rely on a direct linear solver, we split the fourth-order biharmonic term in the Cahn–Hilliard equation into two coupled Helmholtz equations. Thus, we rewrite time-discretized versions of Eqs. (2) and (3) in the following form:

$$M\nabla^2 G^{n+1} - \lambda\phi^{n+1} = f_1, \tag{15a}$$

$$-G^{n+1} + Cn^2\nabla^2\phi^{n+1} = f_2, \tag{15b}$$

where $f_1 = -\phi^n/\Delta t - \mathbf{N^n}(\phi)$, $f_2 = 0$, $\lambda = 1/\Delta t$ and the new intermediate variable $G = Cn\nabla^2\phi$. In these equations, the unknowns G^{n+1} and ϕ^{n+1} must be solved for in a coupled manner.

We solve the two-dimensional Laplace and Helmholtz equations that appear in Eqs. (14) (for pressure field) and (15), respectively, through a very efficient direct solver. The standard central differencing for second-order spatial operators yields coefficient matrices that simplify considerably into a significantly reduced one-dimensional linear system for the present axisymmetric configuration. For planar two-dimensional systems, uncoupled linear equations that can be solved using direct substitution are obtained [32]. For the axisymmetric configuration, the discrete Helmholtz equation obtained from the spatial discretization can be expressed as

$$D_{rr}\psi + \psi D_{zz}^T + \lambda\psi = F, \tag{16}$$

where D_{rr} and D_{zz} denote the discrete operator matrices for the second-order derivative along the radial and axial directions, respectively, with ψ as the unknown variable. Application of the matrix bidiagonalization technique [29] allows us to reexpress this linear system in a substantially simplified form:

$$D_{rr}\psi P + \psi P\lambda + \lambda\psi P = FP, \tag{17}$$

$$(D_{rr} + \lambda)\tilde{\psi} + \tilde{\psi}\Lambda = \tilde{F}, \tag{18}$$

where $D_{zz}^T = P\Lambda P^{-1}$, with P and Λ as orthogonal and diagonal matrices, respectively.

In Eq. (18) we have $\tilde{\psi} = \psi P$ with $\tilde{F} = FP$. It can be easily deduced that Eq. (18) corresponds to a tridiagonal linear system that can be inverted very efficiently using Thomas algorithm. Discretization of the axisymmetric computational domain using N_r and N_z cells along the radial and axial directions, respectively, results in a total of N_z tridiagonal systems of the form given by Eq. (18). Each of these linear systems can be solved independently and in parallel. Thus the original two-dimensional linear system of size $N_rN_z \times N_rN_z$ is reduced to N_z one-dimensional linear subsystems of size $N_r \times N_r$. This reduction therefore results in a significant savings in computational expense as well as memory requirements. Since the computational expense of Thomas algorithm for direct solution of tridiagonal systems scales as $\mathcal{O}(N)$, where N denotes the size of the tridiagonal linear system, the overall computational expense is dominated by the matrix vector multiplications, which scale as $\mathcal{O}(N^2)$. Such matrix vector multiplication operations are required twice, before and after the diagonalization and eventual solution recovery steps (i.e., in calculation of the intermediate $\tilde{F} = FP$ and also the calculation of the final solution $\psi = \tilde{\psi}P^{-1}$). The overall procedure for the solution of the linear system described here is computationally efficient and highly parallelizable. In practice, we typically observe over ten-fold speedups compared with our own implementation of the hypre multigrid solver [33], which relies on OpenMP directives for fast computations on 12-core shared memory processors.

4. Simulation results

Before investigating the deformation dynamics of axially stretching liquid bridges confined between hydrophobic surfaces, we validate our simulation methodology for multicomponent flows that involve contact line motion over a stationary solid boundary. Results from standard tests aimed at assessing the accuracy and robustness of our solver, in simulating two-phase incompressible flows involving high density and viscosity contrasts in the presence of surface tension forces, can be found elsewhere [32].

4.1 *Bouncing water drop test*

To begin with, we simulate the interaction between a freely falling water drop and a hydrophobic solid surface placed underneath it. The drop is located initially at a prescribed distance of two initial diameters from the solid surface with air as the surrounding fluid medium. The principal objective here is to assess the robustness and accuracy of our numerical technique in simulating multicomponent flows involving high density ratios ($\approx$1:10^3), with significantly high surface tension forces and contact line motion.

The simulation is performed on a fixed grid that is used to discretize the time-invariant computational domain $\Omega_{r,z} = [0, L_c] \times [0, 1.5L_c]$. A spherical drop of radius $R_0 = L_c/4$ is centred at $[0, L_c]$ at the beginning of simulation. The velocity of drop is zero initially before it begins to accelerate under the influence of gravity. The direction of gravity is set to $-z$ direction. The top and bottom boundaries of the computational domain are treated as solid walls. A very high static contact angle of 165° is assigned to the bottom boundary. This high contact angle results in hydrophobic characteristics along the bottom wall and leads to a full bounce-back of the impinging drop.

Figure 2 depicts the temporal evolution of the water–air interface, including its initial position (top left frame of

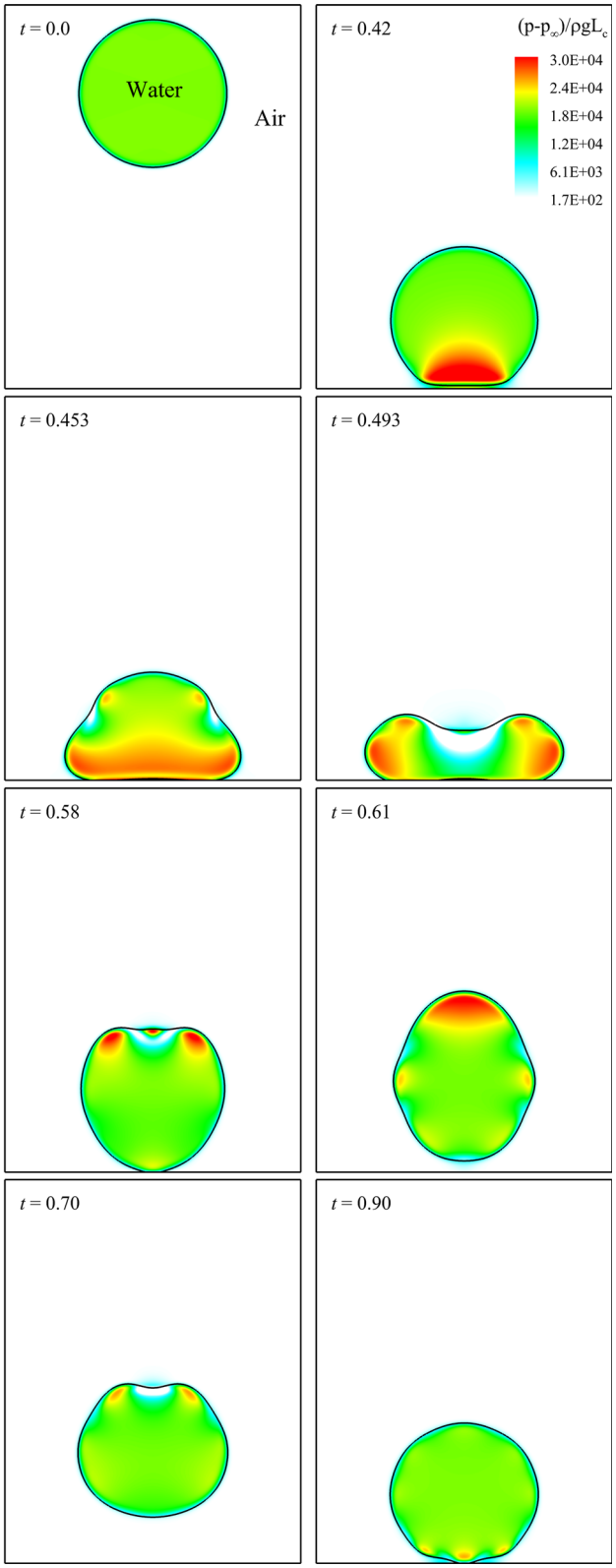

◀**Figure 2.** The water–air interface ($\phi = 0$ isocontour) and the pressure field as a function of time for the bouncing drop test case. The fluid–fluid interface that demarcates the water drop from the surrounding air medium is represented by the *solid black line*. *Colour contours* depict the non-dimensional pressure distribution (pressure has been non-dimensionalized using the inertial scale $\Delta p \sim \rho U^2$, where ρ denotes the density of the water drop and U its terminal velocity.

figure 2), Additional details of this test case, including the physical properties, have been taken directly from [34]. In accordance with [34], we have chosen a density ratio of $\rho_a : \rho_w$ = 1:829, and viscosity ratio of $\mu_a : \mu_w$ = 1:56.29. The relevant non-dimensional parameters are given as follows: Reynolds number Re $(= \rho_a U_c L_c/\mu_a)$ $= 23.29$, Weber number We $(= \rho_a U_c^2 L_c/\sigma) = 4.315 \times 10^{-4}$ and the Froude number Fr $(= U_c/\sqrt{gL_c}) = 0.319$ where ρ_a and μ_a represent the density and viscosity of surrounding air medium, respectively. The computational domain is discretized using 300×450 uniform cells. The width of the diffuse interface is determined by the Cahn number; $Cn = 0.01$ while the Peclet number Pe $(= Cn/M) = 10^2$.

In figure 3, we depict the position of the droplet centre of mass as a function of time. A near-quadratic dependence is observed initially (for non-dimensional time less than about 0.4) and till the point of impact. Beyond a non-dimensional time of about 0.5 the centre of mass of the drop rises as the drop begins to bounce back. For comparison, results from prior investigations of [34] are also included in figure 3. We find our results to be in reasonably good agreement with the ones reported in [34].

4.2 *Spreading of an axisymmetric drop*

Next, we simulate spreading of an axisymmetric drop on a fixed time-invariant computational domain. In this case, the contact line dynamics predominantly determines the droplet shape and the dependence of the spreading radius on time. This test case is especially important since it assesses the effectiveness of our interface capturing technique in accurately and robustly accounting for the contact line motion. Note that our target physical problem concerning extensional dynamics of stretching liquid bridges depends strongly on the contact line dynamics. Additionally, the test case also sheds light on the key issue of convergence of the present contact line treatment with respect to refinements in both mesh spacing and interface thickness (Cahn number, Cn).

In the following, we compute the spreading of axisymmetric drop over a partially wetting surface using our diffuse interface approach and compare our simulation results with the experimental work of Zosel [35]. The configuration considered in the experimental investigation of [35] consists of a small polyisobutylene (PIB) solution (with various concentrations) drop of 1.2–1.5 mm radius, which is allowed to spread on a PTFE (polytetrafluoroethylene) surface. For these settings the static contact angle (θ_s) is approximately 56°. These settings and the associated

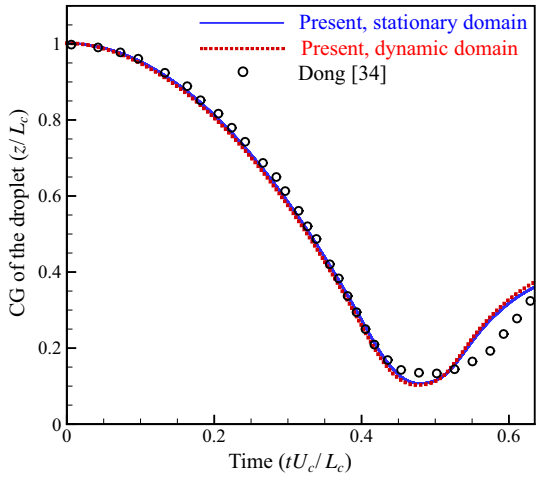

Figure 3. The temporal dependence of the position of the centre of mass of the falling droplet computed from our present simulations compared with the results taken from [34].

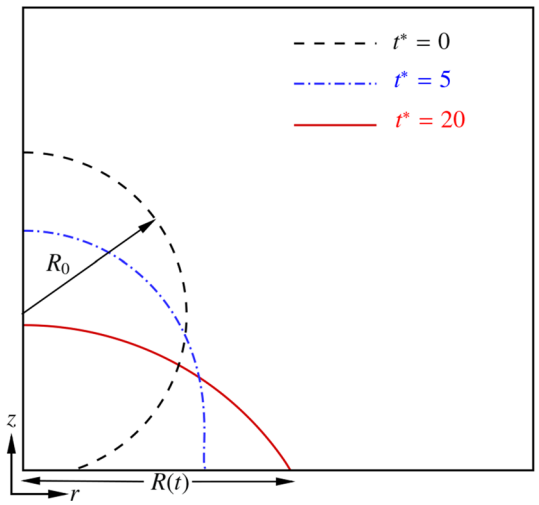

Figure 4. The fluid–fluid interface ($\phi = 0$ isocontour) at successive times for the spreading axisymmetric drop. The initial interface profile (at $t^* = 0$) is depicted using *dashed black lines*.

configuration were also used in the work of Khatavkar *et al* [36] towards validation of their interface treatment technique.

Figure 4 illustrates the fluid–fluid interface ($\phi = 0$ isocontour) for the spreading drop test case at three time instants starting from the initial condition at time $t = 0$. In our simulations, the viscosity ratio (of drop to the surrounding medium) is set to 100 while the density of both the fluid mediums is chosen to be equal. For this surface-tensiondriven test case, we perform non-dimensionalization using the capillary scale for the velocity ($U_{cap} = \sigma/\mu$) and the initial radius of the spherical drop R_0 as the length scale. The capillary number is set equal to unity ($Ca = 1$). Moreover, to closely match the experimental conditions, we set Reynolds number to a small value of 0.1, at which inertial effects are expected to remain substantially low.

To analyze convergence attributes of our interface capturing methodology, we analyse the sensitivity of our results concerning droplet spreading to progressive refinement in the width of the diffuse interface. To perform this analysis we vary the Cahn number (Cn) from 0.01 to 0.0286 along with the corresponding mesh spacing. Such an analysis allows us to draw important conclusions concerning the convergence of the interface capturing technique as the sharp interface limit of the present diffuse interface approach is attained [26]. Furthermore, in this interface width sensitivity analysis, the non-dimensional mobility parameter (M), which determines the relaxation rate of the phase field function to its equilibrium hyperbolic tangent profile, is kept constant at 4×10^{-5} over the entire range of Cn considered in the simulations [26]. We perform simulations over a fixed computational domain $\Omega_{r,z} = [0, 3R_0] \times [0, 2.75R_0]$ and apply outflow boundary conditions on the top and right boundaries. Moreover, we apply symmetry boundary conditions on the left boundary, which coincides with the axis at $r = 0$. On the stationary bottom boundary, we model the wetting characteristics of the solid surface by enforcing a static contact angle of 56°.

The temporal evolution of the dynamic radius $R(t)$ of the spreading droplet normalized with the initial radius of the droplet R_0 is depicted in figure 5 for varying Cn and successively refined computational grids. We find an effective collapse of the normalized dynamic radius profiles with successive interface width refinements. This suggests that our interface capturing methodology does converge towards a sharp interface limit as the interface width is decreased progressively. Furthermore, the dynamic radii for the progressively refined runs are also compared with the experimental data from [35] in figure 5. We observe a reasonably good agreement between the experimental results and the predictions from our simulations. The slight discrepancy between the two results could very likely be due to our choice of $Re = 0.1$, which does not exactly correspond to the inertialess limit considered in the experimental work of [35].

4.3 *Liquid bridge simulations*

Having validated our interface capturing methodology, we now apply our dynamic domain flow solver to compute the extensional dynamics of a liquid bridge located initially between stationary lower and moving upper hydrophobic solid surfaces. The initial shape of the liquid bridge corresponds to a cylindrical column of fixed radius R. The Reynolds and capillary numbers defined using this initial radius of the cylindrical liquid bridge R, and the pulling speed V_c, as the characteristic length and velocity scales, are set to $Re = 1$, $Ca = 0.01$. The density and viscosity ratios (liquid:gas) are fixed at 826.94:1 and 56.29:1, respectively.

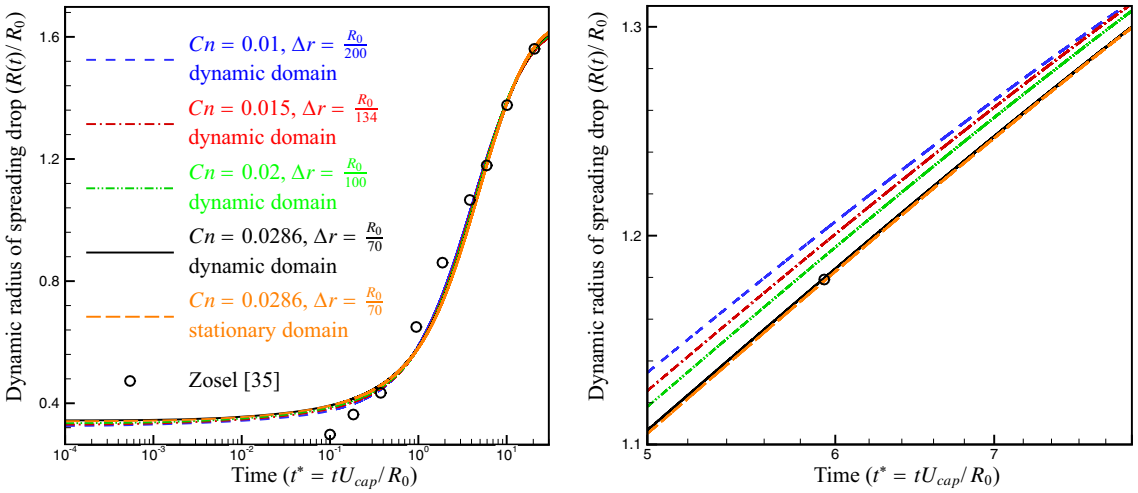

Figure 5. The normalized dynamic radius of the spreading drop $(R(t)/R_0)$ for various Cn as a function of time (non-dimensional time $t^* = tU_{\text{cap}}/R_0$ with $U_{\text{cap}} = \sigma/\mu$), compared with the experimental results of Zosel [35].

Simulations are performed on an axi-symmetric domain $\Omega = [0, 3R] \times [0, 2R]$. The thickness of the diffuse interface is given by the Cahn number $Cn = 0.01$, while the Peclet number ($Pe = Cn/M$) is given by $M \propto 3Cn^2$ (see Magaletti *et al* [37]). The static contact angle on the stationary bottom solid surface is set at $\theta_{\text{bottom}} = 100°$. The top surface is prescribed a slightly higher hydrophobicity through a contact angle of $\theta_{\text{top}} = 120°$.

Figure 6 depicts the fluid–fluid interface ($\phi = 0$ isocontour) along with non-dimensional pressure distribution. The impulsive motion of the top solid surface and the contact line gives rise to capillary waves along the fluid–fluid interface. In time these interfacial capillary waves are gradually damped out owing to the fluid viscosity and a gradual necking of the bridge ensues on the top moving surface. The necking gives way to a complete detachment of the liquid bridge from the top solid surface and eventually the entire liquid adheres to the bottom stationary surface as evidenced from the bottom frames of figure 6.

Next, we interchange the hydrophobicity of the top and bottom surfaces by increasing the prescribed contact angle at the bottom plate to $\theta_{bottom} = 140°$ while keeping the contact angle prescribed at the top plate fixed at $\theta_{top} = 120°$. Figure 7 illustrates the fluid–fluid interface ($\phi = 0$ isocontour) and the corresponding non-dimensional pressure distribution as a function of time for the aforementioned configuration. The evolution of the fluid–fluid interface and the contact line motion is analogous to the previous case considered earlier in that the contact line undergoes significantly larger displacement on the surface with higher hydrophobicity. The bridge necking is therefore observed principally on the surface with higher hydrophobicity (i.e., the bottom stationary surface). As a consequence, in this case the entire liquid bridge fluid eventually adheres to the lower surface.

Next, we consider a configuration in which the contact angle prescribed on the stationary and the moving surfaces are equal ($\theta_{\text{top}} = \theta_{\text{bottom}} = 120°$) so that both the top and the bottom plates are equally hydrophobic. Figure 8 illustrates the fluid–fluid interface ($\phi = 0$ isocontour) and the corresponding non-dimensional pressure distribution as a function of time for this set-up. In this particular case, since the contact angles prescribed at the top and the bottom surfaces are equal, the contact line motion along the top moving and the bottom stationary surfaces are identical and very nearly symmetric, with slight asymmetry attributable to the inertial effects, which are expected to be small but non-vanishing at finite Reynolds number ($Re = 1$). Thus, unlike in the case of previous two configurations, necking and eventual detachment occur along both the top and the bottom surfaces so that eventually the entire liquid bridge fluid undergoes complete detachment with none of it adhering to either of the two solid surfaces.

The deformation dynamics of the liquid bridge are significantly influenced by the contact angle prescribed at the top and moving solid surfaces. This sensitivity of the extensional and detachment dynamics is expected to lead to significant variations in the net force experienced by the top moving and the bottom stationary plates. To quantify the effect of a change in the contact angle prescribed at the bottom stationary plate on the forces exerted on the plate we employ the following expression:

$$F = \int_{\partial\Omega} [-p\mathbf{I} + \mu(\nabla\mathbf{u} + \nabla\mathbf{u}^T)] \cdot \mathbf{ds},$$

to compute the net force F exerted on the solid surfaces. Note that this expression includes all the components of traction forces exerted on the plate. Since the liquid bridge deformation is circumferentially symmetric, the tangential component of the net traction force vanishes identically and only the normal component is non-zero.

In figure 9, we show the total normal force exerted on the top and bottom plates as a function of time for the three

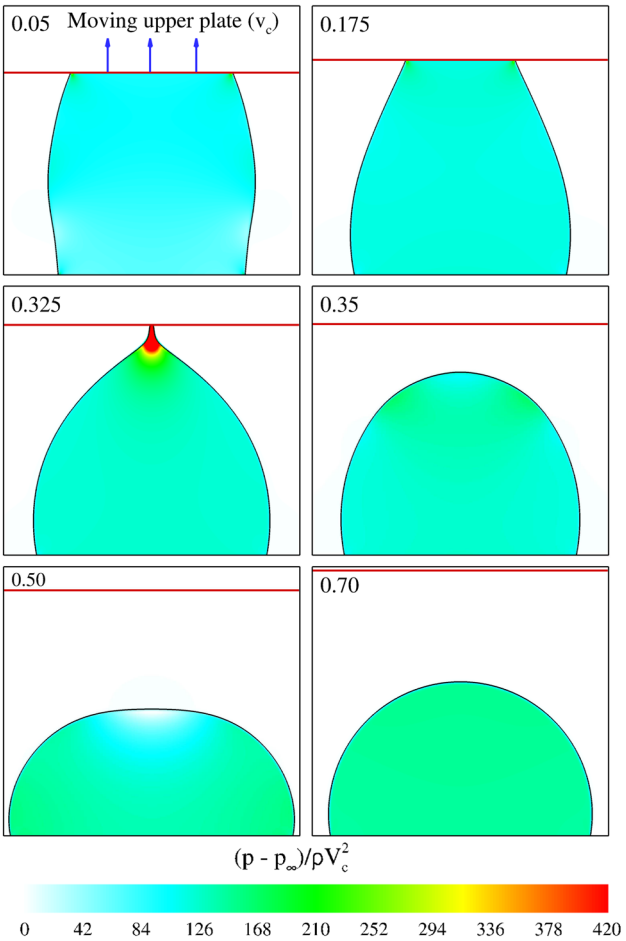

Figure 6. The fluid–fluid interface ($\phi = 0$ isocontour) and the pressure field as a function of time for an axially stretching liquid bridge confined between stationary bottom ($\theta_{\text{bottom}} = 100^\circ$) and moving top plates ($\theta_{\text{top}} = 120^\circ$). The fluid–fluid interface that demarcates the liquid bridge fluid from the surrounding air medium is represented by the *solid black line*. The *straight red line* depicts the top moving plate, which coincides with the upper boundary of the computational domain. *Colour contours* depict the non-dimensional pressure distribution (pressure has been non-dimensionalized using the inertial scale $\Delta p \sim \rho V_c^2$, where ρ denotes the density of the liquid bridge fluid).

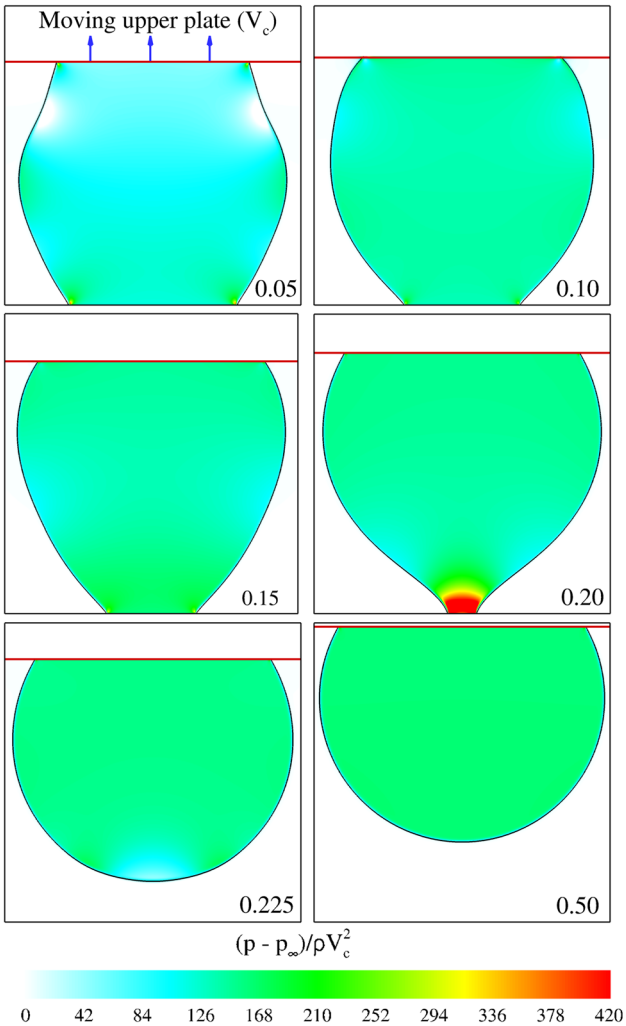

Figure 7. The fluid–fluid interface ($\phi = 0$ isocontour) and the pressure field as a function of time for an axially stretching liquid bridge confined between stationary bottom ($\theta_{\text{bottom}} = 140^\circ$) and moving top plates ($\theta_{\text{top}} = 120^\circ$). The fluid–fluid interface that demarcates the liquid bridge fluid from the surrounding air medium is represented by the *solid black line*. The *straight red line* depicts the top moving plate, which coincides with the upper boundary of the computational domain. *Colour contours* depict the non-dimensional pressure distribution (pressure has been non-dimensionalized using the inertial scale $\Delta p \sim \rho V_c^2$, where ρ denotes the density of the liquid bridge fluid).

configurations with distinct θ_{bottom}. Relatively large temporal variations in the total normal force experienced by the top and the bottom plates are observed for $\theta_{\text{bottom}} = 100^\circ$ and 140° cases, for which the entire fluid adheres to one of the two plates. Furthermore, beyond the point of detachment, the force exerted on the surface with higher hydrophobicity diminishes considerably as the entire liquid bridge fluid adheres to the less hydrophobic surface. In contrast, when $\theta_{\text{top}} = \theta_{\text{bottom}} = 120^\circ$, the temporal variation of the magnitude of the net force exerted on the two plates is very nearly the same (the sign of the force undergoes a complete inversion due to the fact that the normals on the two surfaces point along exactly opposite directions). Moreover, the magnitude of the normal force acting on the two plates decreases gradually with necking and vanishes almost completely beyond the point of complete detachment.

5. Conclusions

In summary, we presented an efficient numerical scheme based on Cahn–Hilliard phase field method coupled with an incompressible Navier–Stokes flow solver to investigate extensional and detachment dynamics of stretching

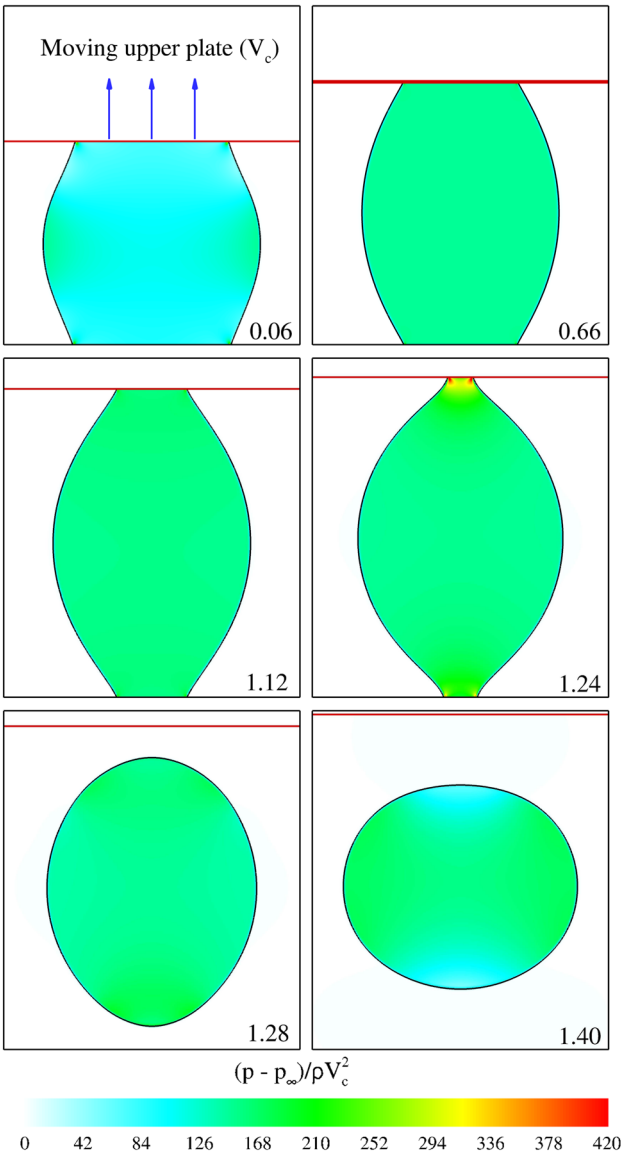

Figure 8. The fluid–fluid interface ($\phi = 0$ isocontour) and the pressure field as a function of time for an axially stretching liquid bridge confined between stationary bottom ($\theta_{\text{bottom}} = 120°$) and moving top plates ($\theta_{\text{top}} = 120°$). The fluid–fluid interface that demarcates the liquid bridge fluid from the surrounding air medium is represented by the *solid black line*. The *straight red line* depicts the top moving plate, which coincides with the upper boundary of the computational domain. *Colour contours* depict the non-dimensional pressure distribution (pressure has been non-dimensionalized using the inertial scale $\Delta p \sim \rho V_c^2$, where ρ denotes the density of the liquid bridge fluid).

liquid bridges. Our general simulation methodology is applicable to physical problems that involve one-dimensional steady or unsteady motion of domain boundaries. Our interface capturing technique effectively handles high density ratios as revealed by the bouncing water drop test case. This test case also establishes the effectiveness of our method in accounting for relatively large contact-angle-induced

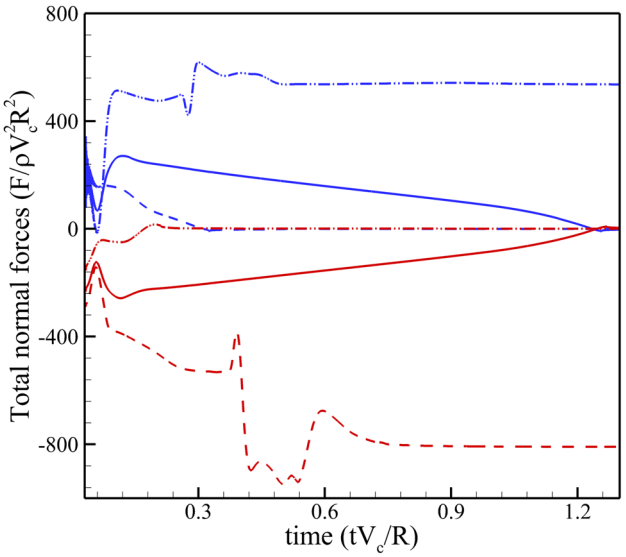

Figure 9. Total normal forces along both top (*blue lines*) and bottom plate (*red lines*) are shown for all three configurations with varying bottom plate contact angle. Along the top plate, the contact angles are kept unchanged at $\theta_{\text{top}} = 120°$, while along the bottom plate they are prescribed as $\theta_{\text{bottom}} = 100°$ (shown by *dash* and *double dots*), 120° (depicted using *solid line*) and 140° (depicted using *dashed lines*).

interfacial deformations (contact angle $\theta_s \sim 165°$) on solid surfaces with high hydrophobicity. Axisymmetric simulations of a continuously stretched liquid bridge showed that our method accurately models the contact line motion in a time-evolving domain with a single moving boundary. Simulations revealed the strong dependence of the liquid bridge extensional and detachment dynamics, and the resulting forces, on the contact angles prescribed at the moving and stationary solid surfaces that contain the liquid bridge.

Acknowledgements

Support provided by the Department of Science and Technology (DSTO 1329) and Supercomputing Education and Research Center-Indian Institute of Science (runtime on Cray XC40) is gratefully acknowledged.

References

[1] Kumar S 2015 Liquid transfer in printing processes: liquid bridges with moving contact lines. *Annu. Rev. Fluid Mech.* 47: 67–94

[2] Fortes M A 1982 Axisymmetric liquid bridges between parallel plates. *J. Colloid Interface Sci.* 88: 338–352

[3] Lambert P 2007 *Capillary forces in microassembly: modeling, simulation, experiments, and case study*. Springer

[4] Eggers J 1997 Nonlinear dynamics and breakup of free-surface flows. *Rev. Mod. Phys.* 69: 865

[5] Qian B and Breuer K S 2011 The motion, stability and breakup of a stretching liquid bridge with a receding contact line. *J. Fluid Mech.* 666: 554–572

[6] Li J, Hesse M, Ziegler J and Woods A W 2005 An arbitrary lagrangian eulerian method for moving-boundary problems and its application to jumping over water. *J. Comput. Phys.* 208: 289–314

[7] Demirdžić I and Perić M 1990 Finite volume method for prediction of fluid flow in arbitrarily shaped domains with moving boundaries. *Int. J. Numer. Meth. Fluids* 10: 771–790

[8] Matallah H, Banaai M J, Sujatha K S and Webster M F 2006 Modelling filament stretching flows with strain-hardening models and sub-cell approximations. *J. Non-Newtonian Fluid Mech.* 134: 77–104

[9] Dodds S, Carvalho M S and Kumar S 2012 The dynamics of three-dimensional liquid bridges with pinned and moving contact lines. *J. Fluid Mech.* 707: 521–540

[10] Marella S, Krishnan S, Liu H and Udaykumar H S 2005 Sharp interface cartesian grid method I: an easily implemented technique for 3d moving boundary computations. *J. Comput. Phys.* 210: 1–31

[11] Udaykumar H S, Mittal R, Rampunggoon P and Khanna A 2001 A sharp interface cartesian grid method for simulating flows with complex moving boundaries. *J. Comput. Phys.* 174: 345–380

[12] Kim D and Choi H 2006 Immersed boundary method for flow around an arbitrarily moving body. *J. Comput. Phys.* 212: 662–680

[13] Jacqmin D 1999 Calculation of two-phase Navier–Stokes flows using phase-field modeling. *J. Comput. Phys.* 155: 96–127

[14] Olsson E, Kreiss G and Zahedi S 2007 A conservative level set method for two phase flow ii. *J. Comput. Phys.* 225: 785–807

[15] Ding H, Spelt P D M and Shu C 2007 Diffuse interface model for incompressible two-phase flows with large density ratios. *J. Comput. Phys.* 226: 2078–2095

[16] Shukla R K, Pantano C and Freund J B 2010 An interface capturing method for the simulation of multi-phase compressible flows. *J. Comput. Phys.* 229: 7411–7439

[17] Shukla R K 2014 Nonlinear preconditioning for efficient and accurate interface capturing in simulation of multicomponent compressible flows. *J. Comput. Phys.* 276: 508–540

[18] Zhang X, Padgett R S and Basaran O A 1996 Nonlinear deformation and breakup of stretching liquid bridges. *J. Fluid Mech.* 329: 207–245

[19] Lee J A, Rothstein J P and Pasquali M 2013 Computational study of viscoelastic effects on liquid transfer during gravure printing. *J. Non-Newtonian Fluid Mech.* 199: 1–11

[20] Huh C and Scriven L E 1971 Hydrodynamic model of steady movement of a solid/liquid/fluid contact line. *J. Colloid Interface Sci.* 35(1): 85–101

[21] Blake T D 2006 The physics of moving wetting lines. *J. Colloid Interface Sci.* 299: 1–13

[22] Qian T, Wang X P and Sheng P 2006 A variational approach to moving contact line hydrodynamics. *J. Fluid Mech.* 564: 333–360

[23] Kusumaatmaja H, Hemingway E J and Fielding S M 2006 Moving contact line dynamics: from diffuse to sharp interfaces. *J. Fluid Mech.* 564: 333–360

[24] Anderson J D 1995 *Computational fluid dynamics: the basics with applications*. McGraw-Hills

[25] Thomas P D and Lombard C K 1979 Geometric conservation law and its application to flow computations on moving grids. *AIAA J.* 17: 1030–1037

[26] Yue P, Zhou C and Feng J J 2010 Sharp-interface limit of the Cahn–Hilliard model for moving contact lines. *J. Fluid Mech.* 645: 279–294

[27] Chorin A J 1968 Numerical solution of the Navier–Stokes equations. *Math. Comput.* 22: 745–762

[28] Tryggvason G, Scardovelli R and Zaleski S 2011 *Direct numerical simulations of gas–liquid multiphase flows*. Cambridge University Press

[29] Peyret R 2002 *Spectral methods for incompressible viscous flow*. Springer, Berlin

[30] Dodd M S and Ferrante A 2014 A fast pressure-correction method for incompressible two-fluid flows. *J. Comput. Phys.* 273: 416–434

[31] Badalassi V E, Ceniceros H D and Banerjee S 2003 Computation of multiphase systems with phase field models. *J. Comput. Phys.* 190: 371–397

[32] Patel K S and Shukla R K A dynamic domain phase field method for simulation of two-fluid incompressible flows. *submitted.*

[33] Falgout R and Yang U 2002 Hypre: a library of high performance preconditioners. *Computational Science ICCS 2002, Lecture Notes in Computer Science* 2331: pp. 632–641

[34] Dong S 2012 On imposing dynamic contact-angle boundary conditions for wall-bounded liquid–gas flows. *Comput. Meth. Appl. Mech. Eng.* 247: 179–200

[35] Zosel A 1993 Studies of the wetting kinetics of liquid drops on solid surfaces. *Colloid Polym. Sci.* 271: 680–687

[36] Khatavkar V V, Anderson P D and Meijer H E H 2007 Capillary spreading of a droplet in the partially wetting regime using a diffuse-interface model. *J. Fluid Mech.* 572: 367–387

[37] Magaletti F, Picano F, Chinappi M, Marino L and Casciola C M 2013 The sharp-interface limit of the Cahn–Hilliard/Navier-Stokes model for binary fluids. *J. Fluid Mech.* 714: 95–126